Available online at website: https://journal.bcrec.id/index.php/bcrec

Bulletin of Chemical Reaction Engineering & Catalysis, 21 (2) 2026, 467-481

Original Research Article

Role of Synthesis Route on The Structural and Photocatalytic Activity of Magnetic TUD-1 Coated $NiFe_2O_4$

Is Fatimah[1,2*], Hiroko Kawaii Wijayanti[1,2], Suresh Sagadevan[3], Sheikh Ahmad Izaddin Sheikh Mohd Ghazali[4], Won-Chun Oh[5], Ruey-an Doong[6]

[1]Department of Chemistry, Faculty of Mathematics and Natural Sciences, Universitas Islam Indonesia, Kampus Terpadu UII, Jl. Kaliurang Km 14, Sleman, Yogyakarta 55584, Indonesia.
[2]Nanotechnology and Sustainable Chemistry Research Centre, Universitas Islam Indonesia, Laboratorium Kimia, Kampus Terpadu UII, Jl. Kaliurang Km 14, Sleman, Yogyakarta 55584, Indonesia.
[3]Nanotechnology & Catalysis Research Centre, University of Malaya, Kuala Lumpur 50603, Malaysia.
[4]Faculty of Applied Sciences, Universiti Teknologi MARA Cawangan Negeri Sembilan, Kampus Kuala Pilah, Kuala Pilah 72000, Negeri Sembilan, Malaysia,
[5]Department of Advanced Materials Science and Engineering, Hanseo University, Seosan-si 356-706, South Korea.
[6]Department of Biomedical Engineering and Environmental Sciences, National Tsing Hua University, Hsinchu, 30013, Taiwan.

Received: 4th February 2026; Revised: 2nd March 2026; Accepted: 3rd March 2026
Available online: 5th March 2026; Published regularly: August 2026

Abstract

In this research, TUD-1 coated $NiFe_2O_4$ was synthesized by comparing *in-situ* and post- synthesis methods, for application as photocatalyst material in dye degradation. One pot synthesis of material was conducted by mixing all chemical precursors in a homogeneous system under hydrothermal condition, followed by calcination at 500°C for 2h. For comparison purpose, two-steps synthesis procedure conducted by firstly synthesis of TUD-1 followed by its use for $NiFe_2O_4$ impregnation. Tetraethyl orthosilicate (TEOS) was employed as precursor for TUD-1 and $NiCl_2.6H_2O$ and $FeCl_3.6H_2O$ were utilized as precursors for synthesis of $NiFe_2O_4$ by co-precipitation method. The physicochemical properties of materials were characterized using X-Ray Diffraction (XRD), Fourier Transform Infrared (FTIR), Gas Sorption Analyzer (GSA), zeta potential, Vibrating-Sample Magnetometry (VSM) and Ultraviolet-Diffuse Reflectance (UV-DRS). The photocatalytic activity examination of materials was conducted for methylene blue (MB) and rhodamine B (RhB) photocatalytic oxidation. The results indicated that in-situ prepared material (NFT-1) produced a higher specific surface area of 228.75 m^2/g compared to post-synthesis material (NFT-2) with the value of 218.07 m^2/g. The NFT-1 material exhibited band gap energy of 2.73 eV which support adsorption capacity and photocatalytic activity. An excellent degradation of MB of 95.67% removal and RhB of 95.08% removal during 60 min were demonstrated by NFT-1. The materials showed magnetism to support easy in separation and reusability. Based on the reusability results, the synthesized material has maintained stability until 5th cycles. Evaluation on the effect of scavengers on the kinetics of photocatalytic degradation has been performed and the hydroxyl radicals (●OH) was proven to be the most important species for the oxidation mechanism.

Keywords: $NiFe_2O_4$; TUD-1; Hydrothermal synthesis; Photocatalyst ; Dyes degradation

How to Cite: Fatimah, I., Wijayanti, H. K., Sagadevan, S., Ghazali, S. A. I. S. M., Oh, W., Doong, R. (2026). Role of Synthesis Route on The Structural and Photocatalytic Activity of Magnetic TUD-1 Coated $NiFe_2O_4$. *Bulletin of Chemical Reaction Engineering & Catalysis*, 21 (2), 467-481. (DOI: 10.9767/bcrec.20665)

Permalink/DOI: https://doi.org/10.9767/bcrec.20665

1. Introduction

Organic-contaminated water is one of the important issues in chemical industries which needs effective and efficient method to treat before released into aquatic environment. For these problems, Advanced oxidation processes (AOPs) are well-known technique including chemical oxidation, photocatalytic oxidation, Fenton, and photo-Fenton methods. The progression to AOPs is related with low-cost, high effective and easy separable catalyst/photocatalyst. Within the scheme, researchers have turned their attention

* Corresponding Author.
Email: isfatimah@uii.ac.id (I. Fatimah)

to iron-based magnetic complex oxides due to their extensive electromagnetic properties[1]. Within the AOPs scheme of methods, photocatalytic degradation has emerged as a cost-effective with high efficiency technology for removing organic compounds-contaminated water including dye-polluted and pharmaceuticals from wastewater [2]. For this purpose, various photocatalysts have been explored with the consideration of chemical stability, reusability and the main features of low cost, high capability to complete in pollutants removal, and easy application at various environmental conditions are needed. Some metal oxide semiconductors such as TiO_2, ZrO_2, ZnO, SnO_2 and their modified forms exhibited their photoactivities towards divers pollutants [2–7].

In larger scale of applications, the use of these photocatalysts faced limitation of the difficulty of photocatalyst separation after the process, and the loss of photocatalytic activity leading to filter clogging and agglomeration, which reduces overall efficiency. To overcome these issues, magnetic materials have gained increasing attention referred to their easy recovery by applying external magnetic field. Spinel-type ferrites MFe_2O_4 (where M can be Co, Cu, Ni, Zn, or Mn) are stand out for their reactivity including in photocatalysis mechanism, high saturation magnetization value, and low toxicity. Within the class of material, nickel ferrite ($NiFe_2O_4$) and its modified form have gained interest to be explored based on their excellent magnetic properties. As photocatalyst, its structure promotes the formation of redox pairs (Fe^{3+}/Fe^{2+} and Ni^{3+}/Ni^{2+}), facilitating charge transfer through a hopping mechanism between cations of different valences, which is the advantageous in the more effective photocatalytic performance [8].

However, pristine MFe_2O_4 nanoparticles dissolve quickly in acidic solution and easy to form aggregates at such reactive functional groups. These conditions allowing metal leaching to the treated solution, which is potentially cause other detrimental contamination to the aquatic environment [9]. Coating $NiFe_2O_4$ by using polymer to modify the surface hydrophobicity and supporting onto high surface area materials, including mesoporous silica are the strategies to overcome the drawbacks [10]. With their high surface area (>800 m^2/g), large pore diameter (2–50 nm), narrow pore size distribution and accessible active sites of surface, mesoporous silica is a promising support. Although silica-coated magnetic nanoparticles attracting much attention for their chemical stability, ease of functionalization with ligands, and ability to form stable dispersions in aqueous media, there are limited number of publications focused on SiO_2-coated $NiFe_2O_4$ nanoparticles [11,12]. In this research, The University of Delft (TUD-1) was chosen as the mesoporous silica. TUD-1 is a three-dimensional mesoporous silicate synthesized in 2001, characterized by an irregular, sponge-like pore structure. The high specific surface area and thermal stability are highly potential to facilitate surface mechanism in catalysis as reported in some previous catalysis and photocatalysis works [13–15].

In term of green chemistry approach, an efficient synthesis procedure could be attempted by minimizing step of preparation procedure. One-pot synthesis of TUD-1-coated $NiFe_2O_4$ nanoparticles is conducted in this work. Facile procedure including the self-assembly formation of $NiFe_2O_4$ nanoparticles in TUD-1 formation environment was proposed. As comparison, two-step synthesis consisting of TUD-1 preparation followed by $NiFe_2O_4$ nanoparticles impregnation was also conducted. The research aimed to evaluate the physicochemical feature of in-situ synthesized material (furthermore called as NFT-1) in comparison with post-synthesis material (NFT-2) and its effect to the photocatalytic activity for dye degradation. Based on the popularity of dye in various industries, methylene blue (MB) and rhodamine B (RhB) were selected as dye model in the photocatalytic activity examination.

2. Materials and Methods

2.1 Materials

Chemicals consist of tetraethyl orthosilicate (TEOS, 98% ACROS), triethanolamine (TEA, 97% ACROS), tetramethylammonium hydroxide (TMAOH, 35% Aldrich), dodecyl amine (DDA), nickel chloride hexahydrate ($NiCl_2.6H_2O$, 98% Merck), ferric chloride hexahydrate ($FeCl_3.6H_2O$, 99% Merck), sodium hydroxide (NaOH, 95% Merck), methylene blue (Merck), rhodamine b (Merck), isopropanol (70%), ethylene diamine tetra acetate (EDTA, 99%), benzoquinone (BQ). All the materials were employed as received without further purification.

2.2. Preparation of TUD-1

TUD-1 mesoporous material was synthesized following the procedure reported by precious work [7,8]. In a typical synthesis, a mixture of TEA and H_2O was added dropwise into TEOS while stirring. Subsequently, TMAOH was added dropwise into the above mixture. After stirring for 2 h, a clear and pale-yellow solution was obtained, with a molar ratio composition of $1SiO_2$: 0.3TMAOH :1TEA: $11H_2O$. The mixture was aged at room temperature for 24 h, followed by drying at 100 ^oC for 24 h. The mixture was placed into a-Teflon-lined autoclave for hydrothermal treatment at 150 ^oC for 4h and then calcined at 500 ^oC for 10 h. After these above steps, purely siliceous TUD-1 was obtained.

2.3. Synthesis of $NiFe_2O_4$/TUD

$NiFe_2O_4$/TUD was obtained with varied synthesis procedure, in situ synthesis and post-synthesis or impregnation method. The in-situ procedure was performed by mixing TEA and H_2O followed by its addition to TEOS under vigorously stirring. Into the mixture, TMAOH was added dropwise, and stirring continued for 2 hours. After that, 1% DDA, $NiCl_2.6H_2O$ and $FeCl_3.6H_2O$ were added, and NaOH solution was added to get pH of 10. The obtained mixture was transferred into a Teflon-lined autoclave for hydrothermal process at 150 °C overnight. The obtained samples were filtered, washed by using water until the pH of filtrate was neutral. After that, the sample was dried in oven to remove the water content before calcined at 500 °C for 2 h. The collected solid was obtained from in-situ and encoded as NFT-1.

In the post synthesis or impregnation procedure, TUD-1 was previously prepared before $NiFe_2O_4$ dispersion onto TUD-1. TUD-1 synthesis procedure was executed referred to previous work [7]. Typically, TEA, TEOS, TMAOH and water were employed as precursors under the molar ratio of $1SiO_2$: 0.5TMAOH : 1TEA : $11H_2O$. Furthermore, TUD-1 was dispersed in a 1% of DDA followed by stirring for 30 minutes to get a homogenous suspension. Into the suspension, solutions of $NiCl_2.6H_2O$ and $FeCl_3.6H_2O$ with the Ni:Fe molar ratio was added, and the pH was set to 10. Furthermore, the similar steps for NFT-1 were taken, and finally the obtained sample from post synthesis encoded as NFT-2. As comparison, $NiFe_2O_4$ was also prepared under the similar synthesis condition within NFT-2. Figure 1 provides the scheme of synthesis procedure.

2.4. Characterizations

Characterizations of the obtained samples were conducted by using x-ray diffraction (XRD) on a Shimadzu X6000 (Tokyo, Japan) instrument using a Ni-filtered Cu-Kα source. The 2θ range used in the measurement was from 10-80° with a step size of 4 °/min. Fourier-Transform infrared (FTIR) was recorded on Perkin Elmer Spectrum Two System L160000A (Singapore). SEM measurements were performed on Hitachi S-4800 Scanning electron microscope (Tokyo, Japan) working at 10 kV. The surface parameters of specific surface area, pore volume and pore radius were carried out on a Quanta Chrome NOVA 1200 instrument (Singapore). The material was degassed at 150 °C for 2 h prior the analysis. Zeta potensial analysis was performed using Horiba SZ-100 (Tokyo, Japan). The UV-Visible diffuse reflectance spectra were recorded on Perkin Elmer Lambda 35 (Massachusetts, USA). For magnetism analysis, vibration sample magnetometer (VSM) was employed LakeShore 7400 (Ohio, USA).

2.5. Adsorption Studies

Adsorption experiments were conducted in a horizontal shaker at room temperature. Typically, about 0.2 g of the NFT-1, NFT-2 and TUD-1 powders were dispersed onto MB and RhB solutions with the concentration of 30 mg/L. The sampling to the treated solution was performed

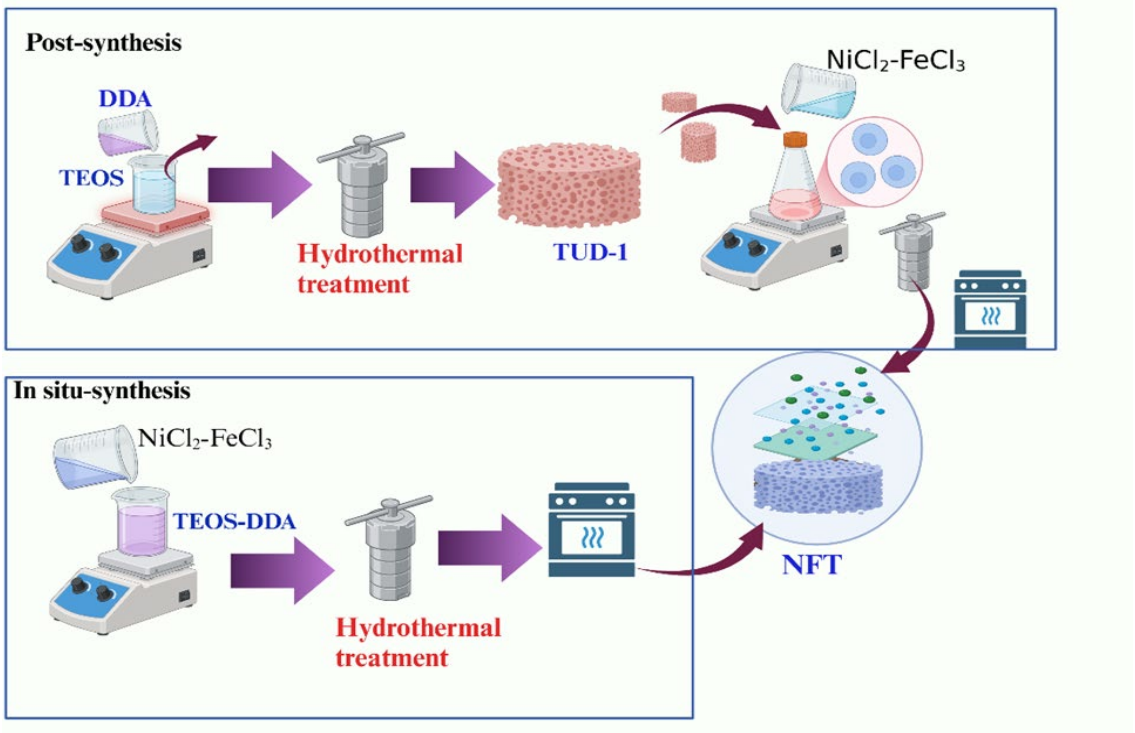

Figure 1. Synthesis procedure of NFT-2 and NFT-1.

sequentially at certain time, and the concentration of solution was analyzed using colorimetric method on UV–Visible spectrophotometry of HITACHI U-2080 (Tokyo, Japan).

2.6. Photocatalytic Activity Examination

The photocatalytic activity examination of NFT-1 and NFT-2 materials were applied for MB and RhB photocatalytic oxidation. For typical photocatalytic experiment, about 0.2 g of material was added into 250 mL of 30 mg/L dye solution. The mixture was placed in a batch photocatalytic reactor equipped with a UV lamp with a wavelength of 296 nm (20 W, intensity of 1.3 mW/cm^2). The adsorption; stirring the mixture in the dark; was performed for 15 min prior the UV light exposure for each experiment. The sampling to the photocatalyzed-solutions was performed sequentially at certain time, and determination of dye concentration was conducted using colorimetric method on UV–Visible spectrophotometry of HITACHI U-2080 (Tokyo, Japan). The effectivity of photocatalytic treatment was measured as the removal efficiency (RE) which was calculated by using the following Equation (1):

$$\text{RE}\ (\%) = \frac{Co - Ct}{Co} \text{ x } 100 \qquad (1)$$

with C_0 and C_t are the concentration of dyes at the initial and time of sampling t.

To determine the participating photoactive material in the mechanism the experiment of MB and RhB adsorption were also employed as comparison. Studies on reusability and stability of samples was conducted on MB photocatalytic oxidation after the sample recycling. The recycling procedure was separation of powder from mixture followed by washing using ethanol:water (1:1) followed by drying in an oven at 100 °C. The photocatalytic mechanism was examined by investigating the influence of IPR, EDTA and BQ addition as the scavengers of •OH, h^+ and •OOH, respectively. Optimization of the scavenger's concentration has been performed and the optimum concentration of IPR, EDTA and BQ are 10 mM, 5mM and 5mM, respectively. At that condition, the interferences on absorbance reading could be minimized. The data from adsorption and photocatalytic experiments were collected by triplicate sampling.

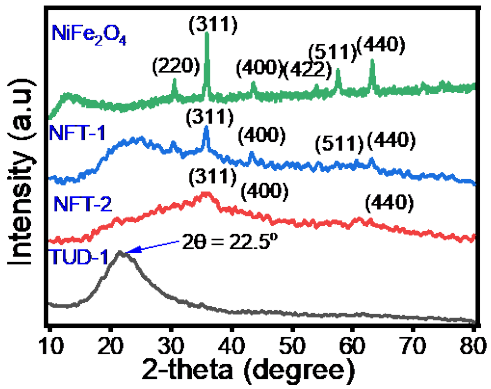

Figure 2. XRD pattern of materials.

3. Results and Discussion

3.1. XRD Analysis

The XRD results of the prepared samples are presented in Figure 2. TUD-1 shows a broad peak at 22.50° as the indication amorphous silica in TUD-1 structure. This result is in confirmation with previous works [13,15]. $NiFe_2O_4$ exhibits the diffraction peaks at 2θ values of 30.53°; 35.89°; 43.58°; 54.04°, 57.58° and 63.2° associated to (220), (311), (400), (422), (511) and (440), respectively. All the observed peaks indicate the formation of spinel $NiFe_2O_4$, confirmed by the standard JCPDS data no. 01-074-2081 [16]. Some of these peaks appeared in NFT-1 are (311), (400), (511) and (440), and the peaks referred to (311), (400), and (440) are indicated in NFT-2. Additionally, both NFT-1 and NFT-2 express the broad peaks ranging at 22-25° which associated to the presence of SiO_2 structure, indicating the formation of nanocomposite. By comparing the peaks exhibited by $NiFe_2O_4$, both NFT-1 and NFT-2 patterns confirm the formation of $NiFe_2O_4$ nanocrystals supported on the SiO_2 layers. The comparison of intensities suggests the lower intensity respect to the crystallinity of prepared $NiFe_2O_4$.

Based on (311) phase of the indication of $NiFe_2O_4$, the crystallite size (D) was calculated by using Scherer equation:

$$\text{D} = \frac{K\,\lambda}{\beta \cos\theta} \qquad (2)$$

With K is reflection constant, λ is the X-ray wavelength, β is full width at half maximum (FWHM) of the reflections, and θ is the reflection angle. Based on the results obtained, it was found that NFT-1, NFT-2, $NiFe_2O_4$ have a crystallite size of 20.02; 19.10 and 1.38 nm, respectively. The crystallite sizes obtained in this research are comparable to $NiFe_2O_4/SiO_2$ by previous works notified the crystallite size ranging at 10-30 nm [17–19]. However, higher compared to [20], which reported a size of 7.80 nm. The crystal size is influenced by several factors, including the synthesis method and the thickness of the silica matrix.

3.2. FTIR Analysis

The FTIR spectra of the samples recorded in the region from 4000 to 400 cm^{-1} are presented in Figure 3. The band of TUD-1 at 3384.23 cm^{-1} indicates the symmetric vibration of the –OH

group from the water molecules in the catalyst system [21]. Following the conversion to NFT-1 and NFT-2, the wavenumbers shift to higher values, specifically to 3419.78 and 3409.06 cm^{-1}, respectively. The bands of NFT-1, NFT-2, and TUD-1 at 1629.08; 1631.02 and 1636.81 cm^{-1} are mainly due to water molecules or hydroxyl groups attached to the silica surface (Si-OH vibrations). Additionally, the absorption band from 1060.73 cm^{-1} in TUD-1 to 1044.52 and 1026.02 cm^{-1} in NFT-1 and NFT-2. These wavenumbers represent the asymmetric vibration of Si–O–Si bond from the tetrahedral SiO_4 [22].

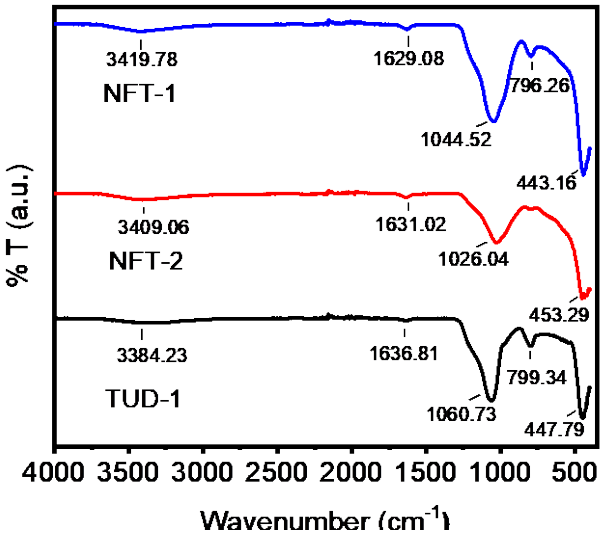

Figure 3. FTIR spectra of TUD-1, NFT-2 and NFT-1.

The wavenumber range of 400-700 cm^{-1} are characteristic of stretching vibrations metal-oxide. The band of TUD-1 is observed at 799.34 cm^{-1} and shifts to 796.26 cm^{-1} in NFT-1. Absorption in this band is due to the symmetric stretching vibrations of Si–O–Si, indicating an interaction between silica and water. In the TUD-1 sample, the peak at 447.79 cm^{-1} corresponds to Si-O bending vibrations. Shi *et al.* [23] reported that a spinel structure of the Ni^{2+}–O bond at the octahedral site is observed at 470 cm^{-1}, while in this study, it was observed at 443.16 cm^{-1} for NFT-1 and 453.29 cm^{-1} for NFT-2 in the spinel structure. These bands are typically associated with ion vibrations within the crystal lattice.

3.3. SEM Analysis

The morphological differences between samples are presented in Figure 4. The samples possessed various particle sizes with a non-uniform particle size distribution; all samples exhibit a porous surface morphology. Figures 4a show a regularly spheric shaped particles characteristic of the mesoporous silica similar to were reported in previous works [24,25]. Supporting $NiFe_2O_4$ onto silica alters the morphology to be a flaky and rougher morphology. In detail, NFT-1 demonstrated a maintained spherical forms surface. Referred to previous study, this kind of form suggesting the silica coating toward $NiFe_2O_4$ particles [26]. The spheric formation is facilitated by the presence of

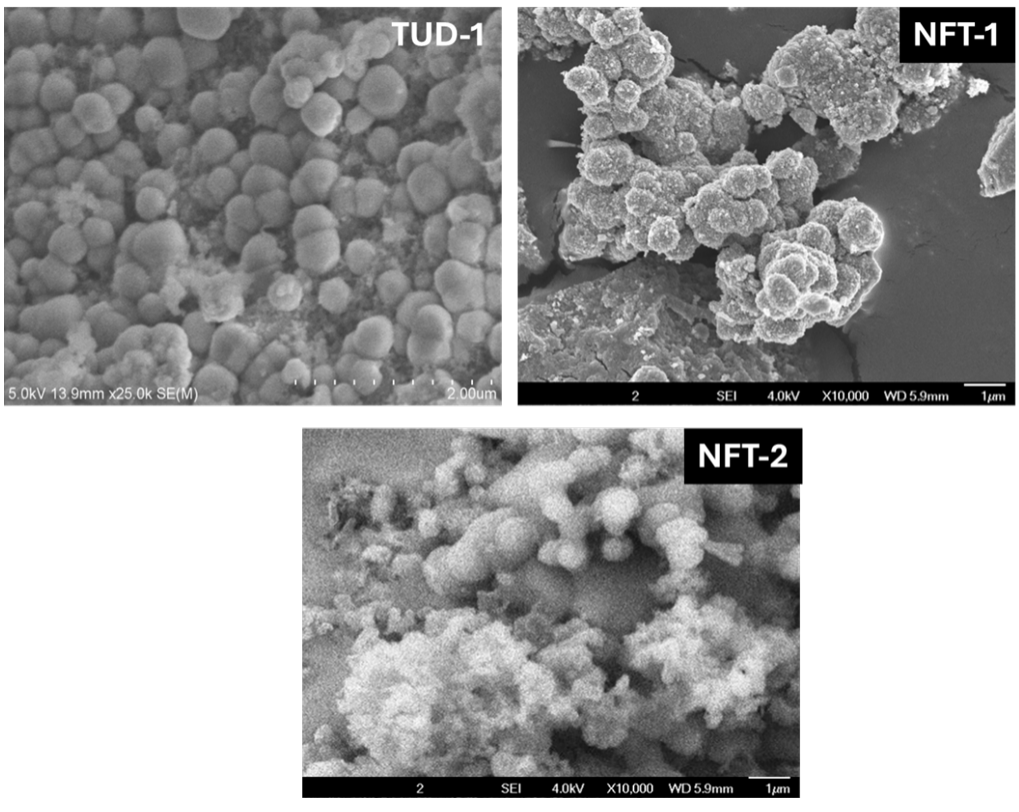

Figure 4. SEM images of (a-b) TUD-1 (c-d) NFT-2 and (e-f) NFT-1.

TMAOH and TEA CTAB as surfactants. Meanwhile, the irregularity of the form is indication of a simulant the crystallite growth of both $NiFe_2O_4$ and SiO_2, which SiO_2 stabilizes the formation of $NiFe_2O_4$ similar to was identified in the synthesis of NiO-SiO_2 [27], SiO_2/α-Fe_2O_3 [28] and Fe_2O_3-SiO_2 [27]. Figure 5 represents the difference between both mechanisms.

3.4. Textural Properties

Textural properties of samples were measured by using gas sorption analysis. The isotherm is presented in Figure 6a. Based on the desorption data, a Barret-Joyner-Halenda (BJH) pore volume distributions of the materials are presented are presented in Figure 6b. The calculated Brunair-Emmet-Teller (BET) specific surface area, pore volume and pore radius are listed in Table 1. The isotherm is identified as of the IUPAC classification with pore sizes ranging from 2-50 nm. Based on the Barret-Joyner-Halenda (BJH) pore size distribution, both materials have the dominant pore sizes of around 2-4 nm, respectively, which are characteristic of the pore diameter in the silica shell [29]. From Table 1, it is known that the specific surface area of NFT-1 is 228.75 m^2/g which higher compared to NFT-2. The results are higher compared to similar material reported in previous works, which surface areas of 86 and 87.75 m^2/g [11,20].

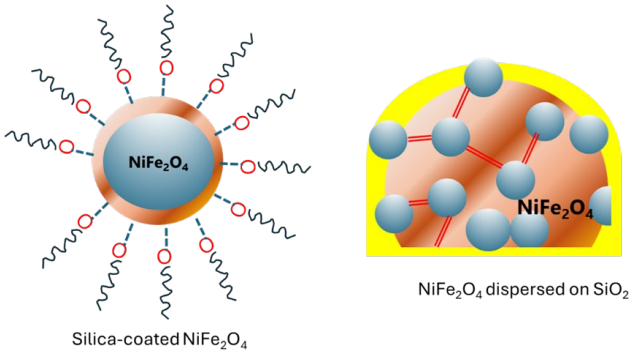

Figure 5. Mechanism of silica-coated $NiFe_2O_4$ and $NiFe_2O_4$-dispersed on SiO_2 formation [26,27].

3.5. Zeta Potential

Zeta potential of materials presented in Figure 7. The zeta potential values of NFT-1, NFT-2 and TUD-1 were -35.2, -28.5 and -17.9 mV, respectively. The negative value indicates that the material's surface tends to attract or retain a negative charge under certain conditions [30]. The sample has ionizable functional groups, such as hydroxyl groups (–OH) on the SiO_2 surface, which can ionize into $–O^-$, and provide a negative charge on the surface. This negative zeta potential results would influence the adsorption of dyes.

3.5. VSM Analysis

The VSM analysis was aimed to study magnetic properties which is correlated to the reusability of the photocatalyst. The magnetic properties of materials are presented in Figure 8. From Figure 8a expressed that NFT-1, NFT-2, and TUD-1 have saturation magnetization (Ms) values of 1.79, 0.91, and 0.22 emu/g, respectively. This indicates that TUD-1 is a non-magnetic material, then with the presence of $NiFe_2O_4$ the

Table 1. Surface parameters from gas sorption analysis of materials.

Parameter	TUD-1	NFT-2	NFT-1
Specific surface area (m^2/g)	280.24	218.07	228.75
Pore volume (cc/g)	0.62	0.50	0.64
Pore radius (nm)	2.43	2.78	3.84

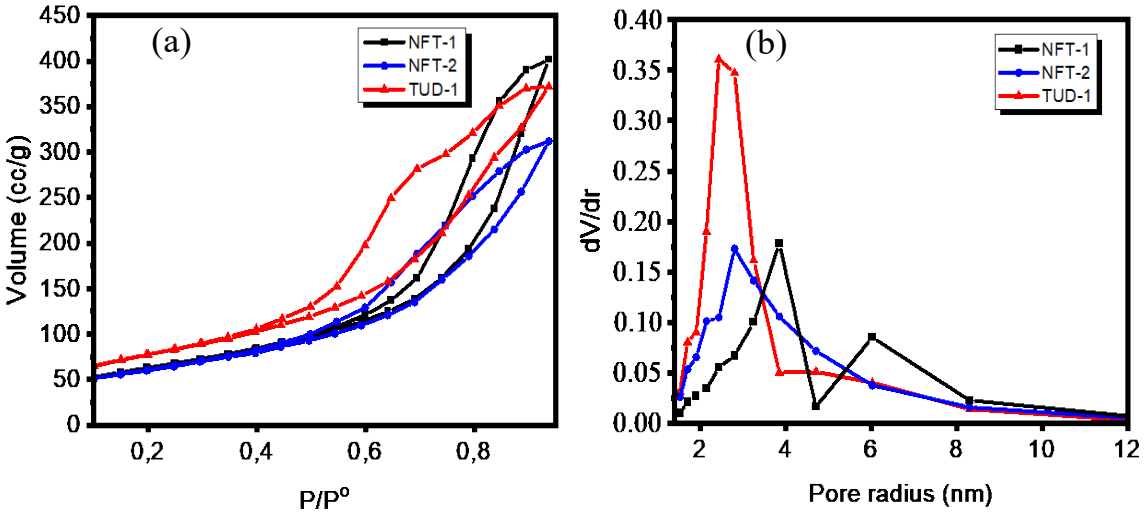

Figure 6. (a). Adsorption-desorption isotherm and (b). pore distribution of NFT-1, NFT-2 and TUD-1.

samples become magnetic. This is relevant with the increased magnetization values observed in NFT-1 and NFT-2.

Based on the magnetic attraction in Figure 7b, NFT-1 can be more easily attracted by a magnet compared to the NFT-2, suggesting the easy separation from the reaction system. Both NFT-1 and NFT-2 exhibit ferrimagnetic characteristics with soft magnetic properties, due to the silica coating in the ferrite nanoparticles. The magnetic properties are influenced by crystal size, which the larger the crystal size, the higher the saturation magnetization [31]. The results of this study are lower than previous research, which reported saturation magnetization values of 20 emu/g for $NiFe_2O_4/SiO_2$ [17].

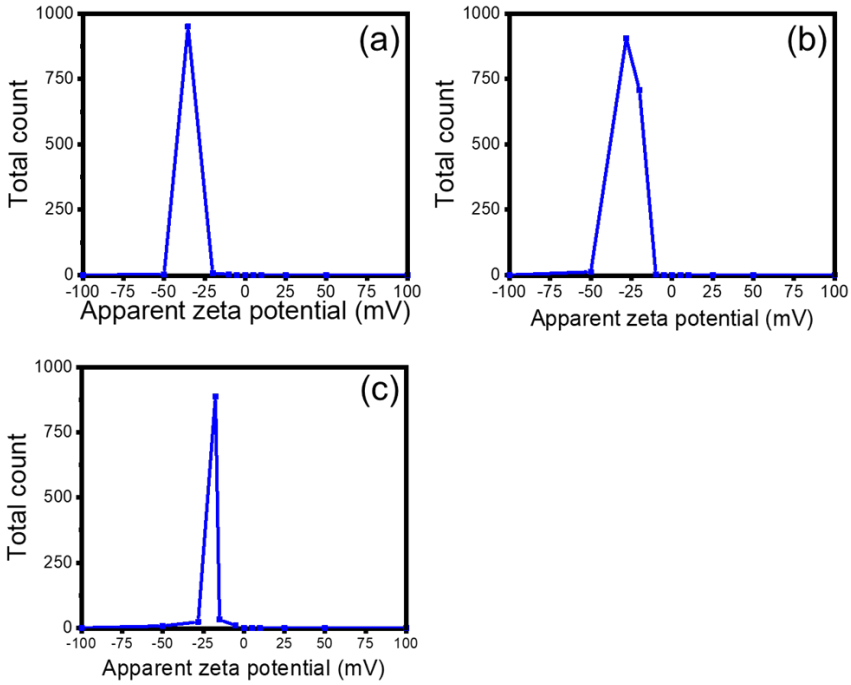

Figure 7. Zeta potential of a. NFT-1, b. NFT-2 and c. TUD-1.

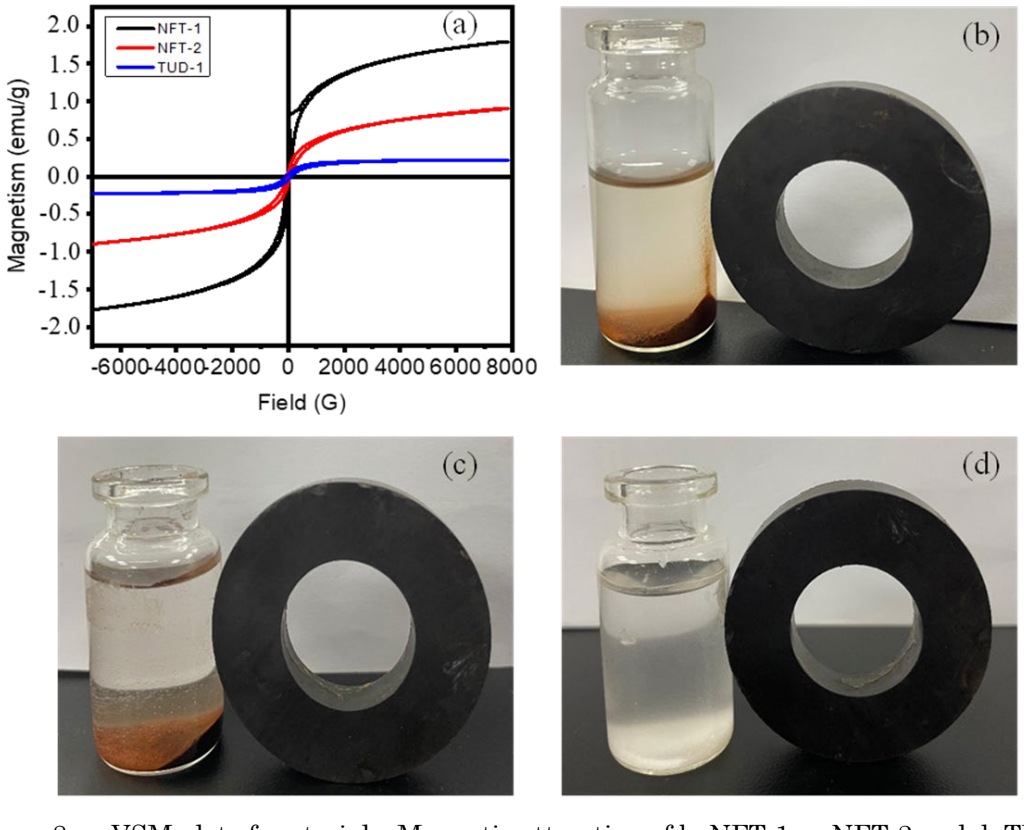

Figure 8. a. VSM plot of materials, Magnetic attraction of b. NFT-1, c. NFT-2 and d. TUD-1.

3.6. Optical Properties

The optical property of materials was evaluated by using UV-DRS spectrophotometry, and the spectrum are presented in Figure 9. It is seen that the band gap values of NFT-1, NFT-2, and TUD-1 are 2.73, 3.11 and 3.19 eV, respectively, for degrade MB and RhB. After TUD-1 was embedded into NFT-1 and NFT-2, the overall band gap of the material decreased. NFT-1 is identified as the superior material due to its smaller band gap, which enhances its photocatalytic activity and increases the degradation of organic compounds. The band gap values of the prepared materials in this study are higher compared to $NiFe_2O_4/SiO_2$ reported in the previous work with the value of 1.67 eV[32]. The band gap energy is influenced by various factors, including particle size, the presence of additional metal ions, and the environmental conditions affecting the atomic structure within the composite [33].

3.7. Adsorption Studies

Adsorption is part of the surface mechanism involved in the photocatalysis mechanism, so it is important to be evaluated. The adsorption kinetics and capacity towards the dyes recognizes whether the photon-activated species contribute significantly to the degradation mechanism or not. In order to evaluate the existing role of materials for adsorption mechanism in decreasing dyes concentration, experiments on adsorption of MB and RhB were performed.

Figure 10a demonstrates the UV-Visible spectral changes of MB and RhB at the initial and treated condition over adsorption using NFT-1 sample. The spectral changes imply the reduced absorbance of treated solution along the increased time of treatment that are corresponding to the reduced concentration. In addition, there is no such spectral shifting which generally confirm the change of molecular structure. Based on the absorbance data at maximum wavelength, the kinetics of MB and RhB adsorption are provided at Figure 10c and Figure 10d, respectively. It is seen that all the samples decrease the dyes concentration, and the reducing concentration is enhanced along the increased adsorption time. The resumed calculations from both plots are represented in Figure 10e which represents that generally the adsorption capabilities of the samples towards both dyes are insignificantly different. It is observed that the adsorption capacities towards MB are higher than that of RhB for all samples. it is seen that the capabilities of the NFT samples to adsorb MB are higher than the capacity towards RhB, meanwhile these are not remarkable different for TUD-1 sample. The more effective MB adsorption is referred to the smaller molecular structure of MB so it has fewer carbon bonds compared to RhB [34]. In addition, the positively-charged the MB structure attracts to be bounded to the negative charges of NFT

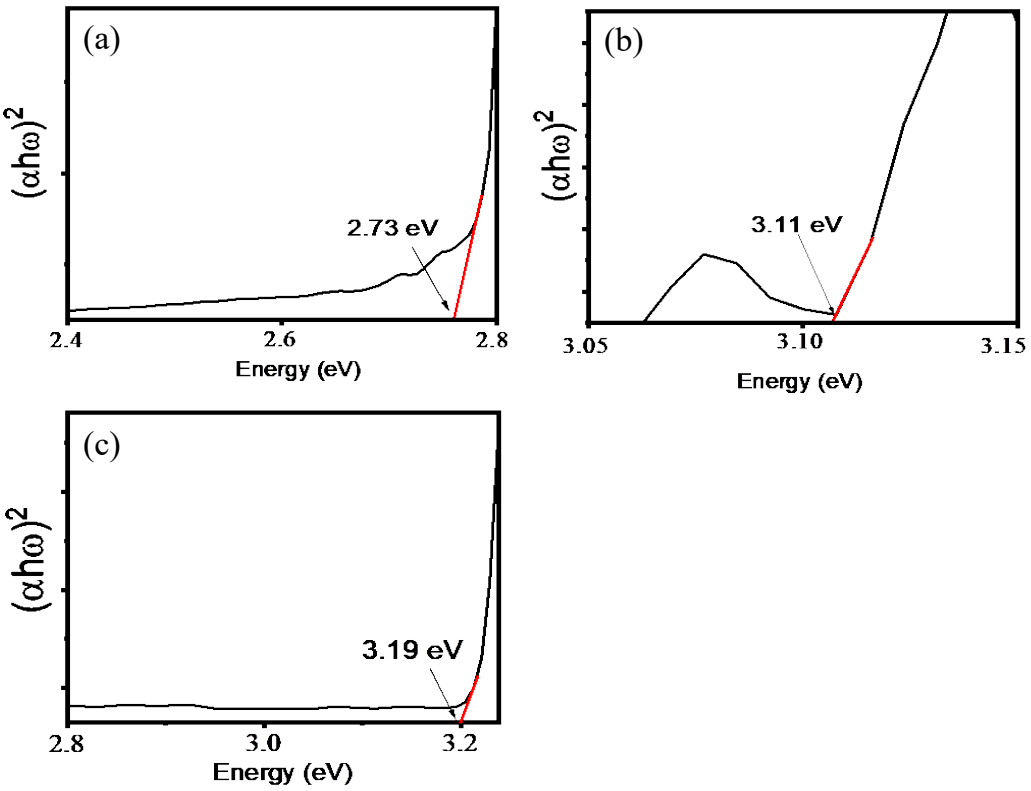

Figure 9. UV-DRS spectra of a. NFT-1, b. NFT-2 and c. TUD-1.

samples surface as expressed by the zeta potential of the samples. This is also confirmed by the order of adsorption capacity of NFT-1 > NFT-2 > TUD-1 which is linear to the most negative charged NFT-1 followed by NFT-2 and TUD-1, respectively.

The adsorption capacity values are comparable and proportional to was reported by previous works on MB adsorption by $NiFe_2O_4$ that showed the adsorption capacity within the range of 1.50-6.15 mg/g for MB concentration ranging at 20-40 mg/L [35]. The adsorption capacities of TUD-1 towards MB and RhB are within range of capacities of the silica samples reported by previous works [36,37]. Based on the adsorption data, pseudo-first order and pseudo-second order adsorption kinetics equations with Equations (2) and (3) were simulated to predict the adsorption kinetics:

$$\ln(q_e - q_t) = \ln q_e - k_1 t \quad (2)$$

$$\frac{t}{q_t} = \frac{1}{kq^2{}_e} - \frac{t}{q_e} \quad (3)$$

with q_e and q_t are the amount of dye adsorbed (mg.g^{-1}), at equilibrium and at a time t, respectively, and k is the rate constant of adsorption kinetics. The calculated parameters are provided in Table 2. From the determination parameters (R^2) it can be concluded that the adsorption kinetics of both dyes using all samples fit to both kinetics equations, confirming that the concentration of dyes determines the adsorption rate. In more detail, pseudo-first order kinetic demonstrates the higher suitability for MB adsorption, meanwhile pseudo-second order kinetic equation is more appropriate for RhB adsorption. Figure 11a-d exhibit the kinetics plots of MB and RhB adsorption.

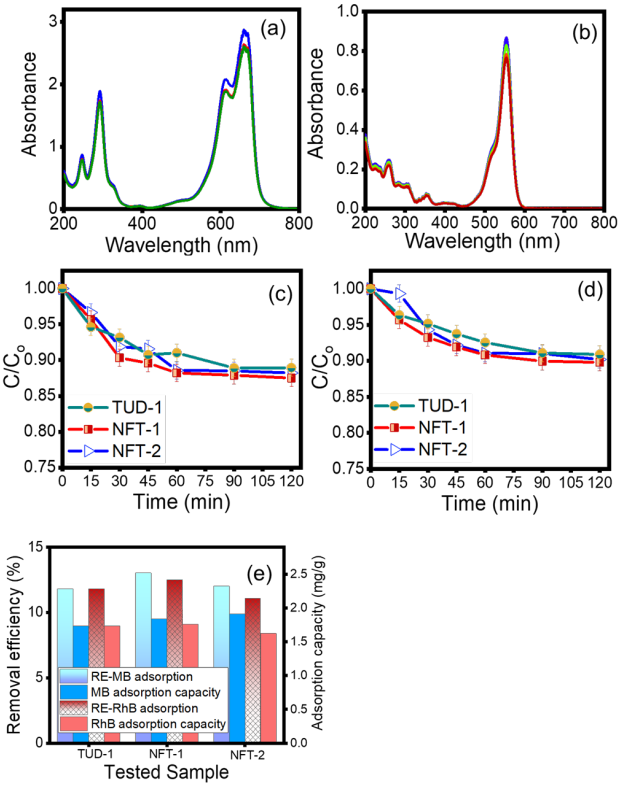

Figure 10. (a-b). UV-visible spectral change by adsorption treatment of MB and RhB, respectively (c-d) Kinetics of MB and RhB

3.8. Photocatalytic Activity Examination

Photocatalytic activity of materials was evaluated on MB and RhB degradation under UV light irradiation. The chosen UV light as photon source in the photocatalytic mechanism refers to the band gap energy of the samples that appropriated to the wavelength ranging at 398-420 nm which positioned at the near UV region.

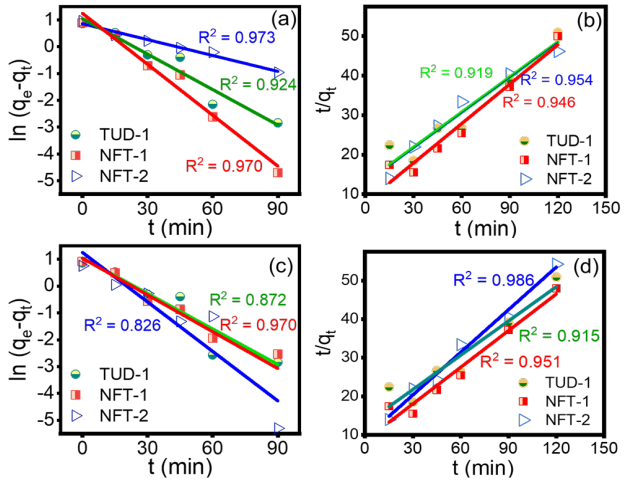

Figure 11. (a-b) Pseudo-first order and Pseudo-second order plots of the MB adsorption, (c-d) Pseudo-first order and Pseudo-second order plots of the adsorption of RhB.

Table 2. Kinetics parameter and equation of adsorption.

Dye	Adsorbent	First-order kinetics (Kinetics equation)	R^2	Second-order kinetics (Kinetics equation)	R^2
MB	TUD-1	$\ln(q_e\text{-}q_t) = -0.055\,t + 1.045$	0.939	$t/q_t = 0.191\,t + 12.955$	0.919
	NFT-1	$\ln(q_e\text{-}q_t) = -0.063\,t + 1.242$	0.976	$t/q_t = 0.332\,t + 7.916$	0.954
	NFT-2	$\ln(q_e\text{-}q_t) = -0.020\,t + 0.855$	0.978	$t/q_t = 0.299\,t + 12.602$	0.946
RhB	TUD-1	$\ln(q_e\text{-}q_t) = -19.644\,t + 24.521$	0.897	$t/q_t = 0.317\,t + 12.877$	0.961
	NFT-1	$\ln(q_e\text{-}q_t) = -0.041\,t + 0.873$	0.960	$t/q_t = 0.369\,t + 8.524$	0.952
	NFT-2	$\ln(q_e\text{-}q_t) = -0.061\,t + 1.252$	0.860	$t/q_t = 0.296\,t + 8.524$	0.915

The UV-Visible spectral change of the initial and photocatalytic-treated MB and RhB solutions using NFT-1 are depicted in Figure 12a and 12b. The spectra demonstrate the reduced absorbance of the MB and RhB initial solutions at 663.5 nm and 546 nm along with longer time of photocatalytic treatment, respectively. Beside this, the shifting of the maximum wavelengths is also identified, suggesting of the solution under the treatments.

The kinetics plots obtained from the photocatalytic treatments using all samples are presented at Figure 12c and 12d, and the resumed RE is provided in Figure 12e. For comparison, the photocatalytic treatments using the prepared $NiFe_2O_4$ were also performed. In addition, the significance of photocatalytic mechanisms is confirmed by the kinetics of photolysis treatments towards RhB and MB provided in Figure 12f. The kinetics plot from photolysis treatments showed that photon exposure without any catalyst could not significantly reduce both dyes due to insufficient energy neither to activate radicals from water splitting nor to cleavage the bonding in dyes molecules. The data is same with was reported on RhB photolysis reported by previous work [38].

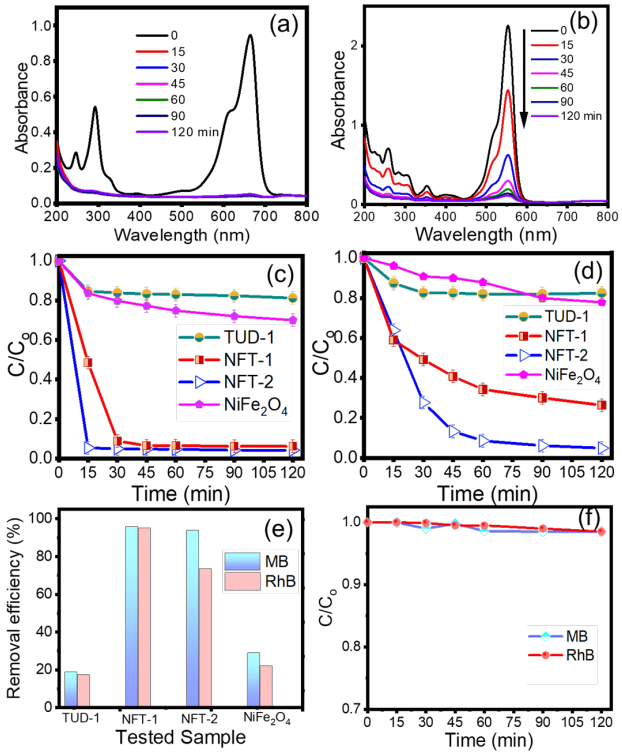

Figure 12. (a-b) UV-Vis spectra of MB and RhB under photocatalytic treatments using NFT-1, (c-d) Kinetics plot of MB and RhB removal under photocatalytic treatments using prepared materials, d. Recapitulated removal efficiency and capacity by photocatalytic treatments, e. Kinetics plot of photolytic treatments [Initial concentration of dye = 30 mg/L, catalyst dose = 0.2 g/250 mL].

NFT samples exhibit the faster removal of both MB and RhB compared to TUD and $NiFe_2O_4$ with following order: NFT-1>NFT-2> TUD-1> $NiFe_2O_3$. In more detail, the capability of NFT samples for removing RhB is higher compared to MB, which is controversially referred to as adsorption capability. In addition, the dyes removal over TUD-1 is in similar values to the removal obtained using adsorption method. The higher photocatalytic activity of NFT-1 rather than NFT-2 is associated with the lower band gap energy of NFT-1 which tends to accelerate the mechanism via faster electron transition for producing hydroxyl radicals for oxidation. In addition, the higher specific surface area, pore volume and pore radius of NFT-1 supports the adsorption step as part of the surface mechanism in photocatalysis. Meanwhile, the removal over TUD-1 is governed only by the adsorption as there is no additional removal value, representing the absence of photoactive material in the solid. The compared photoactivity of NFT samples and $NiFe_2O_4$ implies a remarkable enhanced photocatalytic activity the TUD-1-supported $NiFe_2O_4$. In detail, the in-situ procedure is significantly influencing the mechanism, and technically simpler compared to the synthesis of NFT-2.

More detail analysis to the kinetics data was conducted using pseudo-first order and pseudo-second order kinetics equations (Eqs. (4) and (5)):

$$\ln \frac{c_t}{c_0} = -k_1 t \quad (4)$$

$$\frac{1}{c_t} = k_{obs} t + \frac{1}{c_0} \quad (5)$$

where C_t and C_0 are initial dye concentration and concentration at time of t, and k is kinetics constant.

The kinetic plots are presented in Figure 13, and the calculated parameters are listed in Table 3. The kinetics evaluation gives results that both MB and RhB fit to either pseudo-first order kinetics or pseudo-second-order kinetics equations revealing that the concentration of dye strongly influences the reaction rate [Figure 14]. However, from the R^2 parameters, it is conclusively obtained that the MB degradation over NFT-1 and NFT-2 is more appropriate to the pseudo-first-order kinetics, meanwhile RhB degradation over both NFT samples tends to obey pseudo-second order kinetics. Considering the adsorption kinetics data, the MB is easier to be adsorbed onto NFT samples rather than RhB due to the charge-influenced surface interaction, the role of MB concentration is higher than RhB concentration to accelerate the reaction. The results of RhB photodegradation kinetics are different to was reported on the use of $NiFe_2O_4$/g-C_3N_4 which properly followed pseudo-first-order kinetics. However, the kinetics constants of the

process were within the range of 0.009 min^{-1} - 0.045 min^{-1} depending on the content of $NiFe_2O_4$ in the nanocomposite, and this suitable for the obtained results from this work [39, 40]. In addition, the kinetics of MB photodegradation is comparable to similar works using $NiFe_2O_4$/g-C_3N_4 and ZnO/$NiFe_2O_4$[41, 42]. Beside the band gap energy, the effectiveness of the degradation depends on several factors such as initial concentration of dyes, zeta potential, pore structure, pH of solution and catalyst dosage.

3.8. Reusability

Reusability of catalyst is important features for application. Experiments were conducted over 5 cycles to degrade the MB, presented in Figure 14a. The used catalyst was separated using a magnet, followed by drying at 60 °C before reuse. Furthermore, the photocatalytic process was then repeated under the same treatment and conditions. Based on the results, it is evident that in cycle 1, NFT-1, NFT-2, TUD-1 catalysts produced a lower DE compared to the other cycles. This was due to differences in the UV light source (photon) and the UV-Vis spectrophotometer used. In second use until 5th cycle, each sample showed no significant change of both DE values. DE obtained after 5 cycles for NFT-1, NFT-2, TUD-1 and $NiFe_2O_4$ was 99, 80 and 30%, respectively. This means that the activities of both catalysts are remains stable, which the reduced activity no more than 5%.

The tests of photocatalysis mechanism were conducted to determine the effect of +IPR, +EDTA and + BQ. These addtions were used to predict the role of OH radical (●OH), hole (h^{+}) and superoxide radical ($O_2^{\bullet-}$) scavenger, respectively. From Figure 14b-c it can be seen the addition of scavengers reduced both *RE* and *k* of photocatalytic degradation of MB on NFT-1. The data suggests that all species consist of ●OH, h^+ and $O_2^{\bullet-}$ play role in influencing oxidation mechanism. In more detail, the reductions of the parameters over IPR addition are the most significant compared to the addition of BQ and EDTA.It could be implied that ●OH has greater influence than $O_2^{\bullet-}$ and h^+. The reaction rate will be inhibited, so prevent it from reacted with O_2 or H_2O to produce OOH.

By resuming all the data, it is found that one-pot synthesis of material, which mean the less energy and time-efficient procedure produced the more effective and efficient photocatalyst material for dye degradation. This aligns with the energy efficient principle as part of 12 principles of green chemistry. The recyclability of the material and

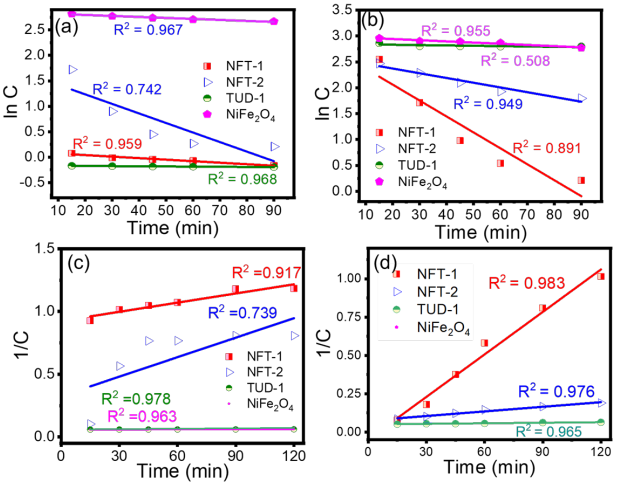

Figure 13. (a-b) Pseudo-first order kinetics plot of MB and RhB photocatalytic degradation, respectively, (c-d) Pseudo-second- order kinetics plot of MB and RhB photocatalytic degradation, respectively.

Table 3. Kinetics parameter and equation.

Dye	Photocatalyst	First-order kinetics (Kinetics equation)	R^2	Second-order kinetics (Kinetics equation)	R^2
MB	NFT-1	$\ln C = -1.87x10^{-2}t + 1.66$	0.958	$\frac{1}{C} = 5.17x10^{-3}\,t + 0.326$	0.917
	NFT-2	$\ln C = -2.99x10^{-3}t + 0.09$	0.742	$\frac{1}{C} = 2.43x10^{-3}\,t + 0.924$	0.739
	TUD-1	$\ln C = -3.22x10^{-4}t - 0.16$	0.968	$\frac{1}{C} = 2.19x10^{-4}\,t + 5.89x10^{-3}$	0.978
	$NiFe_2O_4$	$\ln C = -1.96x10^{-3}t + 2.83$	0.967	$\frac{1}{C} = 1.08x10^{-5}\,t + 5.93x10^{-3}$	0.563
RhB	NFT-1	$\ln C = -3.07x10^{-2}t + 2.68$	0.891	$\frac{1}{C} = 9.24x10^{-3}\,t - 0.047$	0.983
	NFT-2	$\ln C = -9.14x10^{-3}t + 2.55$	0.949	$\frac{1}{C} = 1.00x10^{-3}\,t - 5.51x10^{-2}$	0.976
	TUD-1	$\ln C = -6.75x10^{-4}t + 2.84$	0.508	$\frac{1}{C} = 2.18x10^{-5}\,t - 1.06x10^{-2}$	0.965
	$NiFe_2O_4$	$\ln C = -2.28x10^{-4}t + 2.99$	0.955	$\frac{1}{C} = 1.18x10^{-5}\,t - 1.06x10^{-2}$	0.584

its easily separable after use are the benefits in practicability, bring to the cost-effective technology. The results are potentially developed as a technology for reducing waste and maintaining aquatic environment, that fit to Sustainable Development Goal (SDG) 9 (Industry, Innovation, and Infrastructure) and SDG 13 (Climate Action) by reducing the environmental footprint of chemical processes.

4. Conclusion

R Study on the effect of synthesis route of TUD-1 coated $NiFe_2O_4$ demonstrated that the synthesis procedure significantly influences the physicochemical character and photocatalytic activity of the materials. One-pot synthesized material (NFT-1) represents a mesoporous structured material with higher specific surface area of 228.75 m^2/g compared to two-steps synthesized material (NFT-2) with the value of 218.07 m^2/g. NFT-1 exhibit band gap energy of 2.73 eV to support catalytic activity of MB and RhB. The parameters are contributing factors for the higher adsorption capability of NFT-1 which directly contribute to the higher photocatalytic activity. The removal of MB and RhB by photocatalytic treatment over NFT-1 were 95.67% and 95.08%, respectively. The prepared materials showed easy recyclability and good stability until 5^{th} cycles.

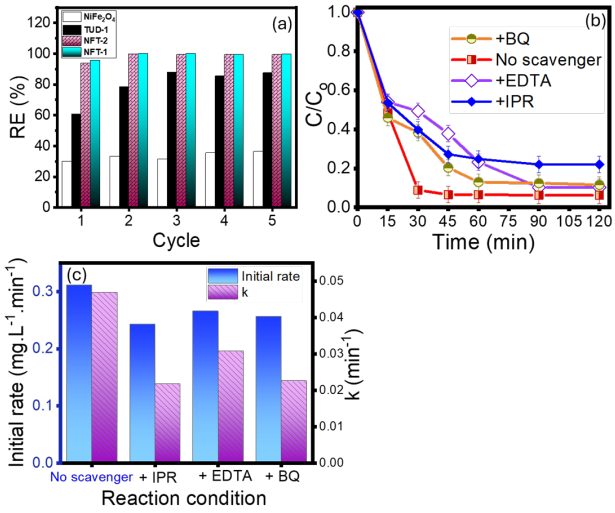

Figure 14. a. RE at reusability test of NFT-1 for photocatalytic degradation of MB, b. Kinetics plot of MB removal using photocatalytic treatment at the addition of scavenger and c. Initial rate and kinetics constant of MB removal using photocatalytic treatment at the addition of scavenger [Photocatalyst: NFT-1, Dye: MB, Initial concentration of dye = 30 mg/L, catalyst dose = 0.2 g/250 mL].

Acknowledgment

Authors thank Department of Chemistry, Universitas Islam Indonesia for supporting this research through Student Mobility Program with NANOCAT, University Malaya.

CRedit Author Statement

Author Contributions: Is Fatimah: Methodology, Resources, Writing, Review and Editing, Supervision, H.K. Wijayanti: Data Curation, Visualization, S Sagadevan: Resource, Visualization, Software, Project Administration , SAISM Ghazali: Validation, Writing, Review and Editing, Data Curation, WC Oh: Validation, Writing, Review and Editing, Data Curation, R Doong: Data curation, Writing, Review and Editing, Supervision. All authors have read and agreed to the published version of the manuscript.

References

[1] Fatimah, I., Fadillah, G., Yudha, S.P. (2021). Synthesis of iron-based magnetic nanocomposites : A review. *Arabian Journal of Chemistry*, 14(8), 103301. DOI: 10.1016/j.arabjc.2021.103301.

[2] Iyyappan, J., Gaddala, B., Gnanasekaran, R., Gopinath, M., Yuvaraj, D., Kumar, V. (2024). Critical review on wastewater treatment using photo catalytic advanced oxidation process : Role of photocatalytic materials , reactor design and kinetics. *Case Studies in Chemical and Environmental Engineering*, 9(November 2023), 100599. DOI: 10.1016/j.cscee.2023.100599.

[3] Ahmadpour, N., Nowrouzi, M., Avargani, V.M., Sayadi, M.H., Zendehboudi, S. (2025). Design and optimization of TiO2-based photocatalysts for efficient removal of pharmaceutical pollutants in water: Recent developments and challenges. *Journal of Water Process Engineering*, 57, 104597. DOI: 10.1016/j.jwpe.2023.104597.

[4] Hussain, R.T., Hossain, M.S., Shariffuddin, J.H. (2024). Green synthesis and photocatalytic insights: A review of zinc oxide nanoparticles in wastewater treatment. *Materials Today Sustainability*, 26, 100764. DOI: 10.1016/j.mtsust.2024.100764.

[5] Madani, H., Saepurahman (2025). Low-energy light-activated Sn2+-SnO2/TiO2 photocatalyst for water pollutant removal. *Journal of Water Process Engineering*, 77, 108425. DOI: 10.1016/j.jwpe.2025.108425.

[6] Bhapkar, A.R., Bhame, S. (2025). A review on ZnO and its modifications for photocatalytic degradation of prominent textile effluents: Synthesis, mechanisms, and future directions. *Journal of Environmental Chemical Engineering*, 12(3), 112553. DOI: 10.1016/j.jece.2024.112553.

[7] Geetha, M., Vashisht, N.B., Thanvir, S., Che, N. (2024). Multi-functional nanoscale ZrO2 catalysts for sustainable water treatment. *Materials Chemistry and Physics*, 316(January), 129096. DOI: 10.1016/j.matchemphys.2024.129096.

[8] Kumar, Y., Karol, V., Awasthi, A., Sharma, A., Kumar, V., Singh, K. (2026). Recent Advancements in Metal Ferrite Hybrid Photocatalysts for Wastewater Treatment. *Trends in Sciences*, 23(4), 11805. DOI: 10.48048/tis.2026.11805.

[9] Saleem, M.U., Hussain, H., Shukrullah, S., Naz, M.Y., Irfan, M., Rahman, S., Ali, A., Ghanim, J. (2024). Study of Kinetics and the Working Mechanism of Silica-Coated Amino-Functionalized CoFe2O4 Ferrite Nanoparticles to Treat Wastewater for Heavy Metals. *ACS Omega*, 93(3), 3507–3524. DOI: 10.1021/acsomega.3c07200

[10] Derakhshani, E., Naghizadeh, A. (2023). Recent advancement in NiFe 2 O 4 -based nanocomposites for the photocatalytic degradation of pollutants in aqueous solutions : a comprehensive systematic review. *AQUA - Water Infrastructure, Ecosystems and Society*, 72 (8), 1629–1645. DOI: 10.2166/aqua.2023.316.

[11] Iqubal, M.A., Islam, S.S., Ghosh, K., Molla, R.A., Kamaluddin, Islam, S.M. (2017). Silica Functionalized Magnetic Nickel Ferrite Nanoparticles as an Efficient Recyclable Catalyst for S-Arylation in Aqueous Medium. *Journal of Inorganic and Organometallic Polymers and Materials*, 27(6), 1730–1739. DOI: 10.1007/s10904-017-0636-3.

[12] Czempik, A., Grasset, F., Auguste, S., Rousseau, Kubacki, J., Sobol, T., Szczepanik, M., Bajorek, N.R.A. (2024). Unraveling the effect of annealing on the structural and microstructural evolution of NiFe2O4@SiO2 core-shell type nanocomposites. *Ceramics International*, 11(8), 20473–20494. DOI: 10.1016/j.ceramint.2024.03.170.

[13] Harjati, F., Citradewi, P.W., Purwiandono, G., Fatimah, I. (2020). Green synthesis of hematite/TUD-1 nanocomposite as efficient photocatalyst for bromophenol blue and methyl violet degradation. *Arabian Journal of Chemistry*, 13(11), 8395–8410. DOI: 10.1016/j.arabjc.2020.05.032.

[14] He, T., Wu, Y., Jiang, C., Chen, Z., Wang, Y., Liu, G., Xu, Z., Ning, G., Chen, X., Zhao, Y. (2020). Novel magnetic Fe3O4/g-C3N4/MoO3 nanocomposites with highly enhanced photocatalytic activities: Visible-light-driven degradation of tetracycline from aqueous environment. *PLoS ONE*, 15(8 August), 1–19. DOI: 10.1371/journal.pone.0237389.

[15] Morad, M., Khder, A.S., Altass, H.M., Moussa, Z., Khder, M.A., Ahmed, A.I., Ahmed, S.A. (2024). Sulfonated mesoporous TUD-1 : An innovative environmentally friendly solid acid catalyst for various organic transformations. *Results in Chemistry*, 8(March), 101583. DOI: 10.1016/j.rechem.2024.101583.

[16] Heikkilä, T., Salonen, J., Tuura, J., Hamdy, M.S., Mul, G., Kumar, N., Salmi, T., Murzin, D.Y., Laitinen, L., Kaukonen, A.M., Hirvonen, J., Lehto, V.P. (2007). Mesoporous silica material TUD-1 as a drug delivery system. *International Journal of Pharmaceutics*, 331(1), 133–138. DOI: 10.1016/j.ijpharm.2006.09.019.

[17] Hamdy, M.S., Mul, G., Jansen, J.C., Ebaid, A., Shan, Z., Overweg, A.R., Maschmeyer, T. (2005). Synthesis, characterization, and unique catalytic performance of the mesoporous material Fe-TUD-1 in Friedel-Crafts benzylation of benzene. *Catalysis Today*, 100(3–4), 255–260. DOI: 10.1016/j.cattod.2004.10.018.

[18] Fatimah, I., Yanti, I., Hana Afiyah Putri, F., Herianto, D., Sagadevan, S., Tamyiz, M., Doong, R. an (2023). Phyto-mediated hydrothermal synthesis of NiFe2O4 as photocatalyst in tetracycline photodegradation. *Environmental Nanotechnology, Monitoring and Management*, 20(August), 100879. DOI: 10.1016/j.enmm.2023.100879.

[19] Eisavi, R., Ghadernejad, S. (2023). NiFe2O4@SiO2–Cu as a novel and efficient magnetically recoverable nanocatalyst for regioselective synthesis of ß-thiol-1,2,3-triazoles under benign conditions. *RSC Advances*, 13, 27984-27996. DOI: 10.1039/d3ra05433k.

[20] Fu, H., Ding, X., Ren, C., Li, W., Yang, H. (2017). composite xerogels for potential application in adsorption of Ce(IV) ions from aqueous solution. *RSC Advances*, (3), 16513–16523. DOI: 10.1039/c6ra27219c.

[21] Sharma, S., Rohilla, S. (2020). Synthesis of nanocomposites of NiFe2O4/SiO2 through coprecipitation method and structural characterization using rietveld refinement. *IOP Conference Proceeding*, 2270, 110023. DOI: 10.1063/5.0020045.

[22] Yulizar, Y., Apriandanu, D.O.B., Zahra, Z.A. (2021). SiO2/NiFe2O4 nanocomposites: Synthesis, characterization and their catalytic activity for 4-nitroaniline reduction. *Materials Chemistry and Physics*, 261(January), 124243. DOI: 10.1016/j.matchemphys.2021.124243.

[23] Alzahrani, E. (2017). Photodegradation of Binary Azo Dyes Using Core-Shell Fe3O4/SiO2/TiO2 Nanospheres. *American Journal of Analytical Chemistry*, 08(01), 95–115. DOI: 10.4236/ajac.2017.81008.

[24] Zhang, S., Dong, D., Sui, Y., Liu, Z., Wang, H., Qian, Z., Su, W. (2006). Preparation of core shell particles consisting of cobalt ferrite and silica by sol-gel process. *Journal of Alloys and Compounds*, 415(1–2), 257–260. DOI: 10.1016/j.jallcom.2005.07.048.

[25] Shi, M., Qiu, T., Tang, B., Zhang, G., Yao, R., Xu, W., Chen, J., Fu, X., Ning, H., Peng, J. (2021). Temperature-controlled crystal size of wide band gap nickel oxide and its application in electrochromism. *Micromachines*, 12(1), 1–11. DOI: 10.3390/mi12010080.

[26] Mehmood, Y., Shahid, H., Siddique, R., Farooq, U., Rizvi, S.M., Uddin, M.N., Kazi, M., Bourhia, M., Dabiellil, F., Mughram, M.H.A.L. (2025). Design and fabrication of a mesoporous silica scaffold for oral delivery of peptides. *Scientific Report*, 15, 29520. DOI: 10.1038/s41598-025-12728-7.

[27] Yuan, M., Zheng, Z., Yu, Y., Wang, Y., Wang, W. (2026). mesoporous silica nanoparticles for advanced cosmetic oil control. *RSC Advance*, 8, 6865–6875. DOI: 10.1039/d5ra08525j.

[28] Eisavi, R., Ghadernejad, S. (2023). RSC Advances NiFe2O4@SiO2 – Cu as a novel and efficient. *RSC Advances*, 13, 27984–27996. DOI: 10.1039/D3RA05433K.

[29] Ali, I., Tahira, A., Ali, M., Hayat, A., Lal, R., Ghaffar, A., Infantes-molina, A., Emo, M., Vigolo, B., Dawi, E., Hussain, Z., Nafady, A. (2026). Development of advanced NiO-SiO2 nanocomposite with flower like morphology , abundant surface oxygen vacancies and enriched Ni 2 + ions for the efficient oxygen evolution reaction and asymmetric supercapacitor applications. *Journal of Energy Storage*, 152(PA), 120652. DOI: 10.1016/j.est.2026.120652.

[30] Lubis, S., Mustafa, I., Ermanda, Y., Ramadhan, M. (2021). Preparation of SiO2/α-Fe2O3 Composite from Rice Husk and Iron Sand as a Photocatalyst for Degradation of Acid Black 1 Dye Preparation of SiO2/α-Fe2O3 Composite from Rice Husk and Iron Sand as a Photocatalyst for Degradation of Acid Black 1. *Journal of Physics: Conference Series*, 1819, 012010. DOI: 10.1088/1742-6596/1819/1/012010.

[31] Shukla, N., Ondeck, A., Lee, J.C., Miller, J.B. (2012). NiFe2O4@SiO2 nanoparticles stabilized by porous silica shells. *Catalysis Letters*, 142(5), 582–587. DOI: 10.1007/s10562-012-0795-3.

[32] Iqubal, M.A., Islam, S.S., Ghosh, K., Molla, R.A., Kamaluddin, Islam, S.M. (2017). Silica Functionalized Magnetic Nickel Ferrite Nanoparticles as an Efficient Recyclable Catalyst for S-Arylation in Aqueous Medium. *Journal of Inorganic and Organometallic Polymers and Materials*, 27(6), 1730–1739. DOI: 10.1007/s10904-017-0636-3.

[33] Yulizar, Y., Apriandanu, D.O.B., Zahra, Z.A. (2021). SiO2/NiFe2O4 nanocomposites: Synthesis, characterization and their catalytic activity for 4-nitroaniline reduction. *Materials Chemistry and Physics*, 261(January), 124243. DOI: 10.1016/j.matchemphys.2021.124243.

[34] Tan, Z., Yuan, S., Hong, M., Zhang, L., Huang, Q. (2020). Mechanism of negative surface charge formation on biochar and its effect on the fixation of soil Cd. *Journal of Hazardous Materials*, 384(February 2019) DOI: 10.1016/j.jhazmat.2019.121370.

[35] Kocan, F. (2021). Preparation and Magnetic Properties of NiFe2O4 Plate Nanoparticles. *Jom*, 73(12), 3702–3709. DOI: 10.1007/s11837-021-04982-7.

[36] Douas, N., Keghouche, N., A. Bilek, H.T., Boutamine, Z. (2024). Enhanced photocatalytic degradation of basic fuchsin using NiFe2O4/SiO2 nanomagnets: synthesis, characterization, and application in wastewater treatment. *Journal of Nanoparticle Research*, 27(4). DOI: 10.1007/s11051-024-06182-1.

[37] Fatimah, I., Wijayanti, H.K., Ramanda, G.D., Tamyiz, M., Doong, R.A., Sagadevan, S. (2022). Nanocomposite of Nickel Nanoparticles-Impregnated Biochar from Palm Leaves as Highly Active and Magnetic Photocatalyst for Methyl Violet Photocatalytic Oxidation. *Molecules*, 27(20), 1–14. DOI: 10.3390/molecules27206871.

[38] Yuliasari, N., Badri, A.F., Siregar, P.M.S.B.N., Palapa, N.R., Mardiyanto, Mohadi, R., Lesbani, A. (2022). Improving the Performance of Mg/Cr LDH by Forming Metal Oxides Mg/Cr-Ni Using Coprecipitation Method as Adsorbent for Cationic Dyes. *Journal of Ecological Engineering*, 23(6), 67–74. DOI: 10.12911/22998993/147837.

[39] Derakhshani, E., Naghizadeh, A., Mortazavi-Derazkola, S. (2023). Phyto-assisted synthesis of magnetic NiFe2O4 nanocomposite using the Pulicaria gnaphalodes methanolic extract for the efficient removal of an antibiotic from the aqueous solution: a study of equilibrium, kinetics, isotherms, and thermodynamics. *Aqua Water Infrastructure, Ecosystems and Society*, 72(11), 2035–2051. DOI: 10.2166/aqua.2023.117.

[40] Hongo, T., Moriura, M., Hatada, Y., Abiko, H. (2021). Simultaneous Methylene Blue Adsorption and pH Neutralization of Contaminated Water by Rice Husk Ash. *ACS Omega*, 6(33), 21604–21612. DOI: 10.1021/acsomega.1c02833.

[41] Silva, J.B.G. e., Rigoti, E., Pergher, S. (2021). Rhodamine B adsorption in ordered mesoporous materials: A comparison efficiency on KIT-6 and CMK-8. *Results in Materials*, 9(November 2020), 100162. DOI: 10.1016/j.rinma.2020.100162.

[42] Bresolin, B.M., Hammouda, S. Ben, Sillanpää, M. (2020). An emerging visible-light organic–inorganic hybrid perovskite for photocatalytic applications. *Nanomaterials*, 10(1), 1–17. DOI: 10.3390/nano10010115.

[43] Mishra, S., Acharya, L., Sharmila, S., Sanjay, K., Acharya, R. (2024). Designing g-C3N4/NiFe2O4 S-scheme heterojunctions for efficient photocatalytic degradation of Rhodamine B and tetracycline hydrochloride. *Applied Surface Science Advances*, 24(August), 100647. DOI: 10.1016/j.apsadv.2024.100647.

[44] Nguyen, L.T.T., Duong, A.T.T., Bui, N.D., Ngo, V.T.M., Nguyen, H.Q., Nguyen, H.T.T., Tran, G.T., Tran, T. Van (2024). Synthesis of magnetic NiFe2O4/g-C3N4 heterojunction photocatalysts for boosting dye degradation performance under visible-light irradiation. *Nanoscale Advances*, 7, 536–548. DOI: 10.1039/d4na00694a.

[45] Stiadi, Y., Wendari, T.P., Zilfa, Zulhadjri, Rahmayeni (2023). Tuning the structural, magnetic, and optical properties of ZnO/NiFe2O4 heterojunction photocatalyst for simultaneous photodegradation of Rhodamine B and Methylene Blue under natural sunlight. *Environmental Engineering Research*, 28(3), 0–3. DOI: 10.4491/eer.2022.074.

[46] Safitri, B., Yohandini, H., Muharni, M., Salni, S., Hariani, P.L. (2024). Synthesis of $NiFe_2O_4$ Magnetic Using Artocarpus altilis Leave Extract for Photocatalytic Degradation of Methylene Blue Dye and Antibacterial Applications. *Jurnal Kimia Sains dan Aplikasi*, 27(8), 371–380. DOI: 10.14710/jksa.27.8.371-380.